Journal of Materials Research and Technology 45 (2026) 6987–6997

Contents lists available at ScienceDirect

Journal of Materials Research and Technology

journal homepage: www.elsevier.com/locate/jmrt

Mechanical behavior of pure Ta exposed to hydrogen at elevated temperatures

Hyojoo Lee [a], Min Ho Kim [a], Min-Jun Cheon [a], Min Cheol Jo [b], Keunho Lee [b], Leeju Park [b], Suk Hoon Kang [c], Sangtae Kim [d], Jungho Shin [e,*], Sangyeob Lee [a,**], Hoon-Hwe Cho [a,***]

[a] Department of Materials Science and Engineering, Hanbat National University, 125 Dongseodaero, Yuseong-gu, Daejeon, 34158, Republic of Korea
[b] Agency for Defense Development, 160 Bugyuseong-daero 488 Beon-gil, Yuseong-gu, Daejeon, 34186, Republic of Korea
[c] Materials Safety Technology Research Division, Korea Atomic Energy Research Institute, 111 Daedeok-daero 989beon-gil, Yuseong-gu, Daejeon, 34057, Republic of Korea
[d] Department of Nuclear Engineering, Hanyang University, 222 Wangsimniro, Seongdong-gu, Seoul, 04763, Republic of Korea
[e] Department of Advanced Materials and Biochemical Engineering, Kangwon National University, 7 Jukheon-gil, Gangneung-si, Gangwon-do, 25457, Republic of Korea

ARTICLE INFO

Keywords:
Tantalum (Ta)
Mechanical response
Interstitial hydrogen
Hydrogen embrittlement

ABSTRACT

Pure tantalum (Ta) is exposed to hydrogen at 10 torr over the temperature range of 400–1000 °C to investigate the effects of hydrogen exposure at elevated temperatures on hydrogen uptake and mechanical response. The Vickers hardness value of the hydrogen-exposed specimens reaches a maximum at 600 °C, and thermal desorption spectroscopy (TDS) analysis confirms a correlation between temperature and hydrogen uptake. X-ray diffraction (XRD) reveals lattice expansion associated with hydrogen incorporation, while scanning Kelvin probe microscopy (SKPM) shows a decrease in surface work function associated with hydrogen dissolution. These results suggest that the observed hardening is most consistent with predominantly interstitial hydrogen together with defect-associated retained hydrogen. Tensile testing further demonstrates that specimens exposed to hydrogen at 600 °C exhibit increased ultimate tensile strength but reduced ductility, accompanied by brittle fracture behavior, indicating the occurrence of hydrogen embrittlement.

1. Introduction

Tantalum (Ta) is a refractory metal with an exceptionally high melting point of 2996 °C and excellent corrosion resistance, which has led to its widespread use in chemical and petrochemical processing equipment, high-temperature heat-exchange systems, semiconductor manufacturing facilities, and other harsh industrial environments [1–5]. Because of its extremely high melting point, most fabrication, heat-treatment, and joining processes for Ta must be conducted at elevated temperatures. Under such conditions, exposure to hydrogen-containing environments is difficult to avoid [6,7].

Hydrogen uptake can occur during several routine manufacturing steps [8–10]. Furnace brazing frequently employs hydrogen-containing reducing atmospheres, and Ta is susceptible to hydrogen-related degradation under such conditions [7,11]. Conventional welding also provides a direct pathway for hydrogen ingress because hydrogen can be introduced from shielding gases, residual moisture, or surface contaminants [12,13].

Ta readily forms hydrides and is therefore susceptible to hydrogen embrittlement when hydrogen is absorbed [7,14]. As the hydrogen concentration increases, hydride formation is promoted; once the solubility limit is exceeded, Ta hydrides precipitate within the lattice. These hydrides are inherently brittle and significantly reduce ductility. In addition, they obstruct slip, thereby facilitating fracture during deformation [13,15–17]. Even below the solubility limit, hydrogen dissolved in Ta can expand the lattice, generate internal stresses, and promote embrittlement[15,18]. Consequently, hydrogen uptake can lead to ductility loss and premature fracture in Ta. Such hydrogen-induced degradation is therefore a major factor limiting the mechanical reliability and industrial applicability of Ta, particularly in environments where hydrogen exposure is unavoidable.

To address these concerns, some studies have examined how

* Corresponding author.
** Corresponding author.
*** Corresponding author.
E-mail addresses: junghos@kangwon.ac.kr (J. Shin), sangyeob@hanbat.ac.kr (S. Lee), hhcho@hanbat.ac.kr (H.-H. Cho).

https://doi.org/10.1016/j.jmrt.2026.10.254
Received 3 July 2026; Received in revised form 21 October 2026; Accepted 27 October 2026
Available online 28 October 2026
2238-7854/© 2026 The Authors. Published by Elsevier B.V. This is an open access article under the CC BY-NC-ND license (http://creativecommons.org/licenses/by-nc-nd/4.0/).

hydrogen uptake and hydride formation influence the strength and ductility of Ta across different temperatures and environments. Spitzig et al. [19] and Owen et al. [20] focused primarily on low-temperature hydrogen embrittlement (−196 °C to room temperature) and reported severe ductility loss accompanied by hydride formation and a ductile-to-brittle transition. At elevated temperatures (room temperature to 816 °C), Walter et al.[21] and Ensinger [22] investigated Ta exposed to mixed H_2O/H_2 combustion gases or corrosive acid environments, where oxidation, corrosion, and hydrogen charging occurred simultaneously. However, these studies did not directly evaluate the bulk mechanical response of Ta under dry hydrogen atmospheres. Although previous work has shown that Ta–H interactions are strongly temperature dependent, studies that directly assess the mechanical behavior of pure Ta under dry, non-oxidizing hydrogen conditions remain limited. The present study aims to elucidate the relationship between temperature-dependent hydrogen retention and the mechanical behavior of pure Ta following exposure to dry hydrogen at elevated temperatures. Such understanding is essential for reliable evaluation of Ta components used in hydrogen-containing environments at elevated temperatures.

In this study, pure Ta was exposed to hydrogen at 10 torr over the temperature range of 400–1000 °C to determine how hydrogen exposure temperature influences hydrogen retention and the associated hardening behavior. Vickers hardness measurements were first used as a screening tool to identify the temperature regime showing the most pronounced hydrogen-associated hardening behavior. To examine the relationship between hydrogen retention, structural changes, and hardening behavior, hydrogen content and trapping behaviors were analyzed by thermal desorption spectroscopy (TDS), while lattice expansion and microstructural evolution were characterized using X-ray diffraction (XRD) and electron backscatter diffraction (EBSD). In addition, scanning Kelvin probe microscopy (SKPM) was employed to probe changes in the surface electronic state associated with hydrogen dissolution. Based on the temperature-dependent screening results, the 600 °C condition, where both retained hydrogen content and hardness reached their maximum values, was used as the principal condition for detailed interpretation of the hydrogen state and its mechanical consequences. Finally, tensile testing was conducted to evaluate the effects of hydrogen exposure on the tensile strength and ductility of pure Ta.

2. Experimental methods

2.1. Materials

As-rolled pure Ta sheets with a thickness of 4.7 mm were sectioned into rectangular specimens measuring 5 mm × 5 mm. These specimens were used as the base material (BM) for all subsequent experiments.

2.2. Hydrogen exposure at elevated temperatures

All hydrogen exposure experiments were conducted in a low-pressure chemical vapor deposition system (LPCVD; LOEs Lab LPCVD-100, South Korea) equipped with a quartz tube, as illustrated in Fig. 1. Fig. 2 schematically shows the thermal histories used for exposures between 400 and 1000 °C. Before heating, the quartz tube was evacuated to approximately 3×10^{-7} torr. The specimens were then heated from room temperature to the target temperature under vacuum. For hydrogen exposure, high-purity H_2 gas was introduced at the target temperature, and the chamber pressure was adjusted to 10 torr. A hydrogen pressure of 10 torr was selected considering the safety requirements for hydrogen exposure at 400–1000 °C and the operating range of the LPCVD system. This pressure was maintained across all exposure temperatures to provide a controlled basis for investigating temperature-dependent hydrogen retention and hardening. The temperature was maintained for 60 min, as indicated by the red line in Fig. 2. The hydrogen exposure time was fixed at 60 min for all temperatures to ensure a consistent comparison of temperature-dependent hydrogen uptake. After the holding period, the H_2 supply was shut off, the chamber was backfilled with Ar, and the specimens were cooled to room temperature under Ar. A reference thermal treatment was also performed using the same vacuum and thermal histories but without hydrogen introduction, as shown in Fig. 2. Under these conditions, the specimens remained under vacuum throughout the entire cycle. This treatment was used to isolate the effect of temperature alone. The hydrogen content after exposure was evaluated by TDS.

2.3. Mechanical testing

Vickers microhardness measurements were performed using a microhardness tester (Duramin-40 M1, Struers, Denmark) to evaluate the surface and cross-sectional hardness of the hydrogen-exposed specimens. Three specimens were examined for each condition. Surface hardness was measured under a load of 0.98 N with a dwell time of 10 s, and the reported value was taken as the average of nine indents spaced at 2 mm intervals. Cross-sectional hardness was measured under the same loading conditions at 10 μm intervals from the edge of the

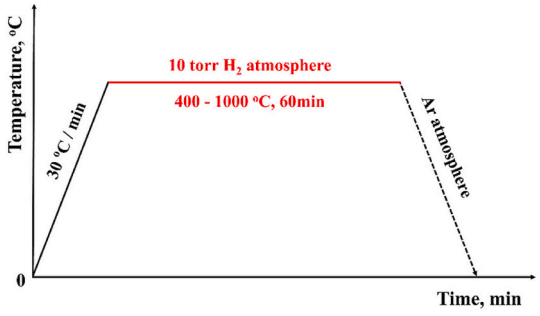

Fig. 2. Schematic illustration of the hydrogen exposure conditions. The black solid line indicates the heating stage, the red solid line represents the hydrogen exposure period, and the black dashed line denotes the cooling stage.

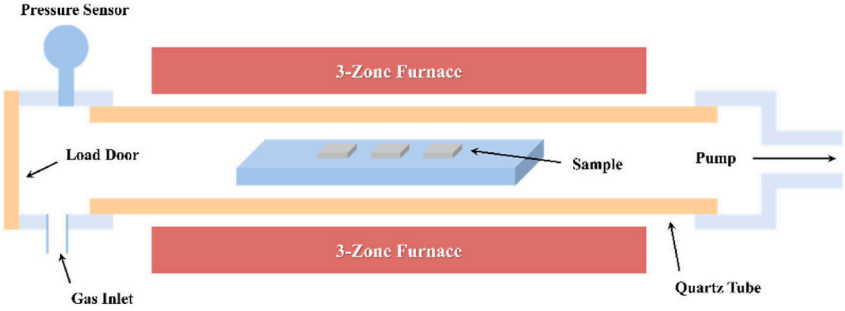

Fig. 1. Schematic illustration of the LPCVD-based experimental setup for hydrogen exposure at elevated temperatures.

specimen, with the value at each depth representing the average of nine measurements.

Tensile tests were conducted at room temperature using a universal testing machine (UTM; RB 301 UNITECH-T, R&B, South Korea). Strain was measured by digital image correlation (DIC; ARAMIS Adjustable 12 M, Zeiss, Germany), which was used as an extensometer. Tensile specimens were machined from the Ta sheets and were subsequently exposed to hydrogen under the conditions shown in Fig. 1. The specimen geometry followed the ASTM E8 subsize standard (Fig. 3) [23]. All tests were performed at a constant nominal strain rate of 1×10^{-3} s^{-1}. After tensile testing, the fracture surfaces of the BM and hydrogen-exposed specimens were examined using scanning electron microscopy (SEM; JSM-IT500, JEOL, Japan).

2.4. Microstructural assessment

Hydride formation in hydrogen-exposed specimens was assessed qualitatively by XRD (SmartLab, Rigaku, Japan) after mechanical grinding and polishing. Measurements were conducted using a Cu Kα X-ray source. To enhance surface sensitivity, grazing-incidence XRD (GIXRD) was performed at a fixed incident angle of 1.2°.

The microstructural characteristics of hydrogen-exposed specimens were examined using field-emission SEM (FE-SEM; JSM-7100F, JEOL, Japan) equipped with an EBSD (TSL Hikari Super, TSL, USA) system. Before EBSD analysis, the polished specimens were subjected to final chemical–mechanical polishing with colloidal silica.

2.5. TDS and SKPM measurements

TDS measurements were performed using a commercial system (HTDS-004, R-DEC, Japan) to evaluate hydrogen desorption behavior, total hydrogen content, and trapping characteristics. Total hydrogen content was quantified by integrating the hydrogen desorption-rate signal over the measurement range. For a constant heating rate, the cumulative hydrogen content was calculated according to the following relationship [24,25]:

$$C_H = \int_{t_0}^{t_f} r_H(t)\, dt = \frac{1}{\beta}\int_{T_0}^{T_f} r_H(T)\, dT \quad (1)$$

where C_H is the cumulative hydrogen content, r_H is the hydrogen desorption rate, t and T denote time and temperature, respectively, t_0 and t_f are the initial and final times of the measurement, T_0 and T_f are the corresponding initial and final temperatures, and $\beta = dT/\,dt$ is the heating rate. One TDS measurement was performed per exposure condition under high vacuum (≈6.2×10^{-8} Pa) at a constant heating rate of 90 °C h^{-1}. To further investigate the hydrogen desorption behavior of the specimen exposed to hydrogen at 600 °C, additional TDS analyses were conducted at heating rates of 180 and 360 °C h^{-1}. The desorption spectra obtained from the 600 °C specimen at the three heating rates (90, 180, and 360 °C h^{-1}) were deconvoluted into individual peaks using Gaussian peak fitting. The apparent desorption activation energy for each peak was determined from Kissinger plots.

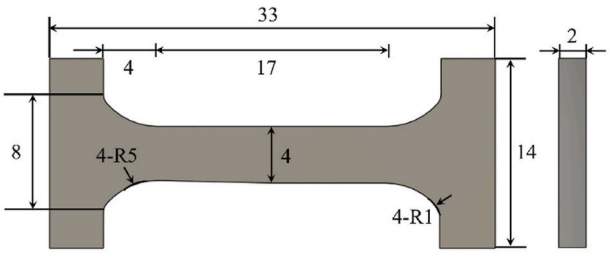

Fig. 3. Geometry of the uniaxial tensile test specimen of the Ta plate (all dimensions in mm).

SKPM measurements were carried out using an atomic force microscope (MFP-3D Infinity, Asylum Research, USA) operated in SKPM mode to evaluate the effect of hydrogen on the surface electronic state of Ta. Before the measurement, hydrogen-exposed specimens were sequentially polished with 3 μm, 1 μm, and 0.25 μm diamond pastes to remove the outermost surface layer and reduce surface roughness. The contact potential difference (V_{CPD}) was mapped using a Pt-coated conductive tip, and the resulting surface potential maps were used to assess hydrogen-induced changes in the surface electronic state.

3. Results and discussion

3.1. Temperature-dependent hydrogen content and hardness

Fig. 4a compares the hydrogen content measured by TDS with the calculated equilibrium hydrogen solubility as a function of hydrogen exposure temperature. The BM contains only a few ppm of hydrogen. After hydrogen exposure, the hydrogen content increases to approximately 11 ppm at 400 °C and about 20 ppm at 500 °C, reaching a distinct maximum of roughly 65 ppm at 600 °C. With further increases in exposure temperature, the hydrogen content decreases to about 46 ppm at 700 °C, around 29 ppm at 800 °C, and to approximately 22 ppm or less above 900 °C. The increase in hydrogen uptake between 400 °C and 600 °C can be associated with changes in the barrier properties of the passive Ta_2O_5 film. Previous studies have reported that the Ta_2O_5 layer remains relatively dense at approximately 400 °C, thereby providing an effective barrier to hydrogen ingress [26,27]. As the temperature increases, however, changes in the oxide structure and stability may reduce its protective capability. Other studies have shown that the

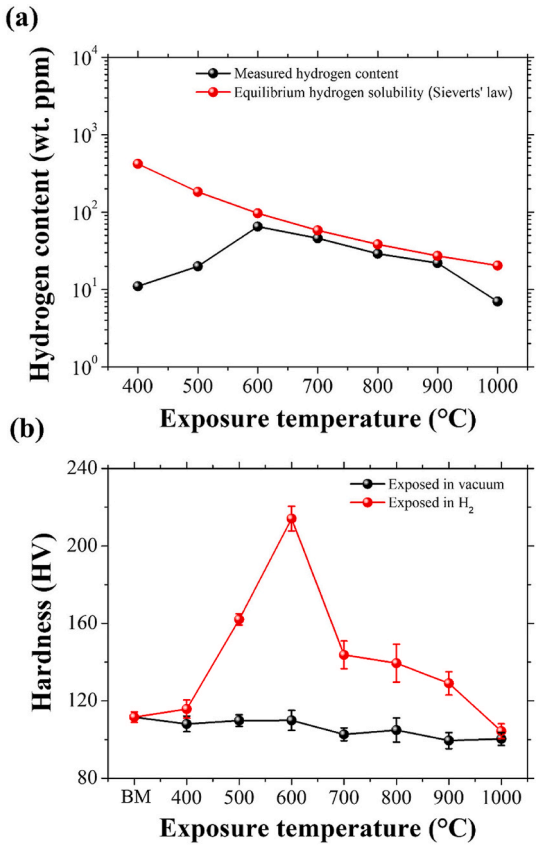

Fig. 4. (a) Hydrogen content as a function of hydrogen exposure temperature (400–1000 °C) measured by TDS, and the corresponding equilibrium hydrogen solubility calculated based on Sieverts' law at a hydrogen pressure of 10 torr. (b) Vickers hardness values as a function of exposure temperature under hydrogen and vacuum atmospheres, including the BM.

mobility of oxygen ions in Ta_2O_5 increases markedly above approximately 500 °C, leading to the generation of oxygen vacancies and increased structural disorder within the oxide layer[28–30]. Such changes may reduce the barrier capability of the oxide film and thereby facilitate the ingress of atomic hydrogen into the underlying Ta. Therefore, the pronounced increase in hydrogen uptake toward 600 °C may be partly associated with temperature-dependent changes in the surface oxide barrier. Above 600 °C, the hydrogen content decreases with temperature. At elevated temperatures, thermally activated recovery processes reduce the density of lattice defects, including dislocations and vacancy clusters that serve as hydrogen trapping sites. As the number of available trapping sites decreases, the hydrogen retention capacity of the material is correspondingly reduced, leading to a lower measured hydrogen concentration [31,32]. In addition, under a fixed hydrogen pressure, the equilibrium hydrogen solubility in Ta decreases with increasing temperature [33,34]. To further interpret the decrease in hydrogen content above 600 °C, the experimental results were compared with the theoretical equilibrium solubility calculated from Sieverts' law at a hydrogen pressure of 10 torr. Under this condition, the equilibrium relationship is expressed as follows [15,35,36]:

$$K\sqrt{P_{H_2}} = C_H \tag{2}$$

$$K = \exp\left(-\frac{\Delta G^0}{RT}\right) \tag{3}$$

where C_H is the concentration of dissolved hydrogen in Ta, P_{H_2} is the hydrogen gas pressure, K is the temperature-dependent equilibrium constant, ΔG^0 is the standard free energy for hydrogen dissolution [34,37], R is the gas constant, and T is the absolute temperature. The calculated equilibrium hydrogen solubility decreases monotonically with increasing temperature, whereas the measured hydrogen content increases up to 600 °C and then decreases at higher exposure temperatures (Fig. 4a). These differences indicate that the retained hydrogen content is not governed by equilibrium solubility alone, while the decrease in both quantities above 600 °C suggests that the thermodynamic decrease in hydrogen solubility contributes to the reduction in retained hydrogen at higher temperatures. Therefore, the decrease in hydrogen content above 600 °C can be interpreted as resulting from the combined effects of two factors: a reduction in hydrogen trapping capacity arising from thermally activated recovery and a thermodynamic decrease in hydrogen solubility with increasing temperature. Furthermore, the enhanced hydrogen diffusivity at elevated temperatures facilitates hydrogen redistribution and desorption, thereby further reducing the amount of hydrogen retained in the lattice [38,39]. At the highest exposure temperature of 1000 °C, the further decrease in retained hydrogen may also be associated with more pronounced thermally activated recovery of the Ta matrix, which can further reduce the density of dislocations and other defect-related hydrogen trapping sites [40,41]. This decrease in solubility implies that the thermodynamic stability of hydrogen in solid solution is reduced at elevated temperatures, and hydrogen may be redistributed into other states, including residual trapping or, in principle, precipitated forms [34,42].

A similar trend is observed for the surface hardness of the hydrogen-exposed samples (Fig. 4b). The hardness increases markedly between 400 °C and 600 °C and reaches a maximum at 600 °C, followed by a gradual decrease at higher temperatures. The results obtained under vacuum conditions, where hydrogen exposure is excluded, are also shown for comparison. Specimens heated under vacuum exhibit a gradual decrease in surface hardness with increasing temperature, from 111.61 ± 2.68 HV for the BM to 100.35 ± 3.36 HV after exposure at 1000 °C under vacuum. The observed decrease in hardness is attributed to a reduction in dislocation density resulting from thermally activated recovery, which diminishes both the contribution to mechanical strengthening and the density of hydrogen trapping sites [39,43]. The hydrogen-exposed specimens exhibit higher surface hardness than those subjected only to thermal treatment, indicating hydrogen-induced surface hardening [44–46]. However, the specimen exposed to 1000 °C under hydrogen exhibits similarly low hardness to that exposed to the same temperature under vacuum, suggesting that the combined effects of reduced hydrogen content and recovery-induced dislocation annihilation contribute comparably in both cases. Specimens exposed between 600 and 1000 °C exhibit a similar decreasing trend in hardness with increasing temperature.

Cross-sectional Vickers hardness profiles were measured for the BM and hydrogen-exposed specimens to assess hydrogen penetration depth and the associated hydrogen-induced hardening at selected temperatures (500, 600, and 700 °C), corresponding to regimes below, at, and above the maximum hydrogen uptake (Fig. 5). The hydrogen penetration depth was estimated from the cross-sectional hardness profiles as the depth at which the hardness approached the BM hardness level. The estimated depth represents the region in which hydrogen-induced hardening was detectable, while lower concentrations of hydrogen may still be present at greater depths. The specimen exposed at 500 °C shows a surface hardness of approximately 160 HV, which gradually decreases to about 110 HV within a depth of roughly 50 μm, approaching the BM hardness. This behavior indicates that hydrogen is primarily localized near the surface at this temperature because diffusion is limited, resulting in a shallow hardened layer. At 600 °C, the hardening effect becomes much more pronounced. The surface hardness reaches approximately 210 HV and gradually decreases with depth, returning to the BM hardness at a depth of about 90 μm. In contrast, the specimen exposed at 700 °C exhibits a reduced surface-hardening effect and a notably smaller hardness gradient. This result indicates that hydrogen is distributed more broadly rather than remaining concentrated near the surface, thereby reducing the near-surface hardening effect. Despite the lower total hydrogen uptake, the penetration depth is greatest among the three specimens because of the enhanced hydrogen diffusivity. These results indicate that hydrogen-induced hardening is most pronounced at 600 °C, as reflected by the surface hardness, whereas the penetration depth reaches its maximum at 700 °C owing to enhanced hydrogen diffusivity.

3.2. Microstructural analysis

Fig. 6 shows inverse pole figure (IPF) and kernel average misorientation (KAM) maps for the BM and for specimens exposed at 600 °C either under high vacuum or under 10 torr hydrogen. The EBSD analyses were performed on cross-sections from the hydrogen-exposed surface. The BM exhibits a recrystallized, equiaxed grain structure (Fig. 6a) [47]. The IPF maps show that this equiaxed morphology is largely preserved

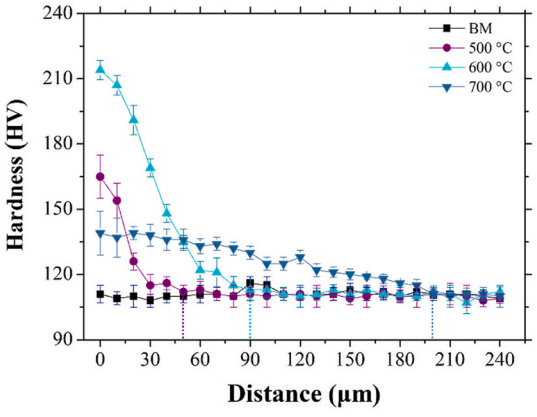

Fig. 5. Vickers hardness values as a function of distance from the surface at different exposure temperatures (500, 600, and 700 °C). The vertical dashed lines indicate the estimated depths of detectable hydrogen-induced hardening at each exposure temperature.

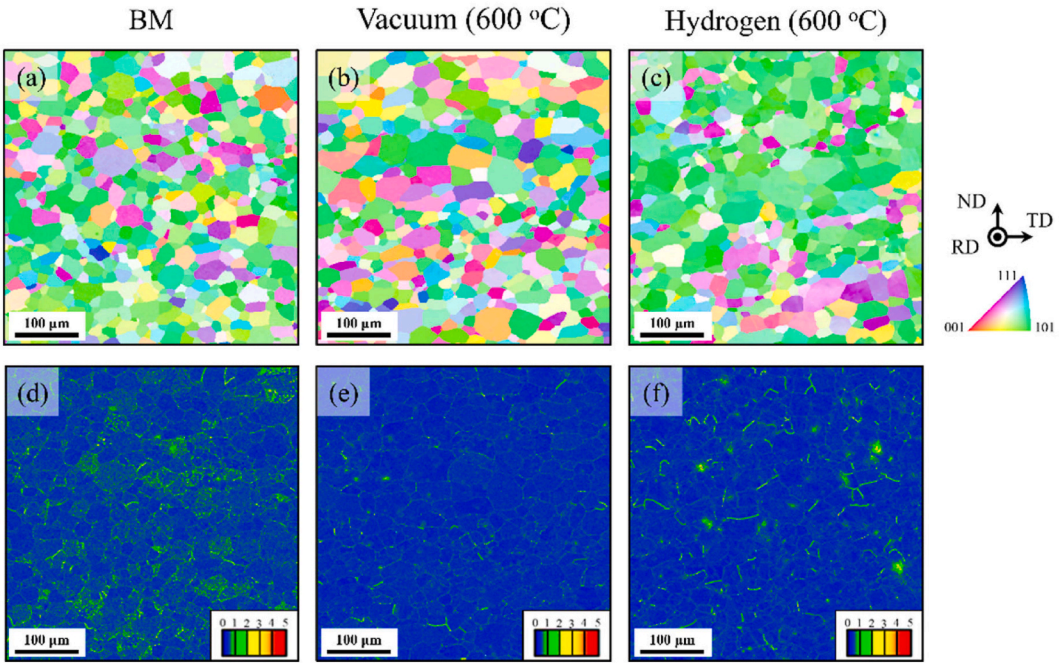

Fig. 6. Microstructural features comparing the BM with Ta specimens processed at 600 °C under vacuum and hydrogen atmospheres. (a–c) RD–IPF maps and (d–f) corresponding KAM maps.

after elevated-temperature exposure in both environments (Fig. 6b and c). No abnormal grain growth or obvious microstructural differences are observed in the hydrogen-exposed specimen relative to the specimen exposed to vacuum at the same temperature. Instead, only slight grain coarsening is detected. The average grain size increases modestly from 27.2 ± 16.3 μm in the BM (Fig. 6a) to 32.4 ± 18.1 μm and 32.5 ± 17.2 μm after exposure at 600 °C under hydrogen and vacuum, respectively (Fig. 6b and c). The corresponding KAM maps are shown in Fig. 6d–f. The BM shows the highest average KAM value (0.44) (Fig. 6d). After elevated temperature exposure, the average KAM values decrease to 0.24 and 0.27 under the hydrogen and vacuum conditions, respectively (Fig. 6e and f). The comparable grain sizes and similar reductions in KAM in the hydrogen-exposed and vacuum-treated specimens suggest that thermal exposure is the dominant factor underlying the observed changes in these parameters [48,49]. The additional contribution of hydrogen to the measured final grain size and local lattice misorientation is therefore considered relatively minor under the present conditions. The modest grain coarsening is associated with thermal exposure, whereas the decrease in KAM is interpreted primarily as reflecting recovery-related relaxation and rearrangement of dislocation structures. Here, KAM serves as a comparative indicator of dislocation-related local lattice misorientation rather than a direct quantitative measure of total dislocation density [50,51].

XRD analysis was performed to identify possible hydride formation and to evaluate the lattice response to hydrogen exposure (Fig. 7). As shown in Fig. 7a, all specimens, including those exposed to hydrogen between 400 and 1000 °C, exhibit only the fundamental reflections of bcc Ta. No β- or ε-type Ta hydride reflections are detected within the instrumental resolution. In addition, the diffraction peaks of the specimens exposed at 500 and 600 °C are shifted toward lower diffraction angles relative to the BM (Fig. 7b and c). According to Bragg's law, this shift corresponds to an increase in lattice spacing and therefore indicates

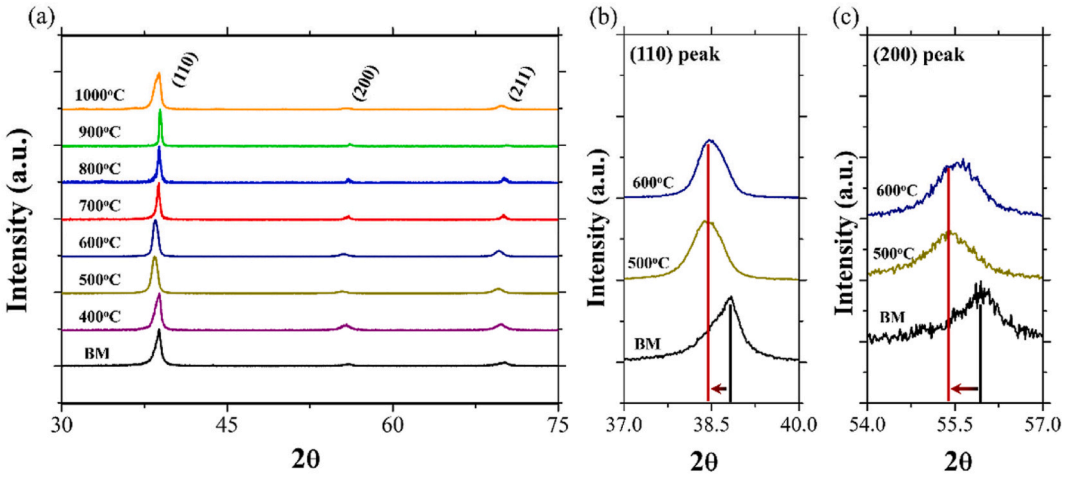

Fig. 7. (a) XRD patterns of the BM as a reference and Ta specimens exposed to a hydrogen atmosphere at temperatures ranging from 400 to 1000 °C. (b, c) Enlarged views of the (110) and (200) diffraction peaks, respectively, comparing the BM with specimens exposed to hydrogen at 500 and 600 °C. The vertical reference lines indicate the peak positions of the BM, highlighting the shift of the diffraction peaks toward lower angles after hydrogen exposure.

lattice expansion of the Ta matrix. A quantitative analysis based on Bragg's law was conducted using the (110) and (200) diffraction peaks. The (110) peak, which exhibits the highest intensity, shifts from 38.8° in the BM to 38.4° after hydrogen exposure. This shift corresponds to an increase in interplanar spacing from 2.325 Å to 2.347 Å. Accordingly, the lattice parameter increases from 3.288 Å to 3.318 Å, corresponding to a lattice expansion of approximately 0.030 Å (~0.9%). For the (200) diffraction peak, the peak position shifts from 55.9° in the BM to approximately 55.5° after hydrogen exposure. This shift corresponds to an increase in interplanar spacing from 1.647 Å to 1.658 Å. Accordingly, the lattice parameter, calculated from the (200) reflection, increases from 3.294 Å in the BM to 3.316 Å after hydrogen exposure, corresponding to a lattice expansion of approximately 0.022 Å (~0.7%). This expansion is attributed to hydrogen atoms occupying interstitial sites within the bcc Ta lattice [36,52].

The hydrogen concentration at each temperature was quantified by TDS, yielding a maximum value of approximately 65 ppm at 600 °C (Fig. 4a), which corresponds to a dilute hydrogen regime. Despite this low hydrogen concentration, a measurable lattice expansion is observed, indicating that even small amounts of interstitial hydrogen can induce a measurable lattice response in Ta. This interpretation is consistent with previous density functional theory (DFT) studies of the Ta–H system [53], which show that hydrogen incorporation into interstitial sites leads to lattice expansion through coupled electronic and atomic interactions. According to the Ta–H phase diagram, hydrogen is expected to be retained predominantly in solid solution within the bcc Ta phase under the present temperature conditions [54,55]. Therefore, the observed lattice expansion is mainly attributed to interstitial hydrogen incorporation, while its temperature dependence reflects the competition between hydrogen ingress, redistribution, and desorption from the lattice, rather than being governed solely by hydrogen concentration. However, the presence of very fine hydride precipitates cannot be completely excluded within the detection limit of XRD.

3.3. SKPM and TDS analysis

To verify hydrogen dissolution and its effect on the surface electronic state, SKPM analysis was performed on the BM and on the specimen exposed to hydrogen at 600 °C (Fig. 8). SKPM measures the V_{CPD} between a conductive probe with a fixed work function and the specimen surface; variations in V_{CPD} reflect changes in the surface work function [56,57]. The BM shows an average V_{CPD} of approximately 0.72 V (Fig. 8e), whereas the hydrogen-exposed specimen exhibits a higher V_{CPD} of about 1.02 V (Fig. 8g). This increase in V_{CPD} indicates a decrease in the specimen work function after hydrogen exposure. The decrease in work function suggests a modification of the electronic band structure associated with hydrogen incorporation into interstitial sites. Interstitial hydrogen may alter the local electron density and thereby contribute to the observed reduction in work function [53,58,59]. This interpretation is consistent with band structure calculations for Ta–H systems, in which hybridization between H 1s states and the Ta 5d band shifts the Fermi level upward and reduces the work function with increasing hydrogen concentration [53,60,61]. SKPM therefore provides surface-sensitive evidence that hydrogen is incorporated into the Ta lattice and modifies the electronic state. These results are also consistent with the XRD results, which show lattice expansion associated with interstitial hydrogen.

TDS analysis was performed on the specimen exposed to hydrogen at 600 °C to identify the hydrogen states associated with the observed lattice expansion and hardness increase. The measured TDS response reflects the retained hydrogen state after exposure and cooling. As shown in Fig. 9a–c, the desorption spectra obtained at different heating rates exhibit a single broad peak, indicating overlapping hydrogen-desorption processes [62–64]. Microstructural and phase analyses suggest that hydrogen is retained primarily as dissolved hydrogen in the bcc Ta lattice under the present conditions. To resolve the overlapping desorption behavior, each spectrum was deconvoluted into two Gaussian components, and the peak temperatures were used for Kissinger analysis (Fig. 9d). The apparent activation energy (E_a) associated with each desorption peak was determined from the slope of the Kissinger plots according to the Kissinger equation [65]:

$$-\frac{E_a}{R}=\frac{\partial \ln\left(\phi/T_p^2\right)}{\partial\left(1/T_p\right)} \tag{4}$$

where R is the gas constant, ϕ is the heating rate, and T_p is the peak temperature of each Gaussian component. Thus, the activation energies are obtained directly from the linear fits of $\ln\left(\phi/T_p^2\right)$ versus $1/T_p$.

The analysis yields activation energies of 81.0 kJ mol^{-1} and 104.7 kJ mol^{-1}, suggesting at least two overlapping retained-hydrogen states. These values fall within the range reported for defect-associated hydrogen trapping in Ta and are therefore consistent with trapping at sites of different binding strength [66–68]. Both values are substantially lower than those typically associated with hydride decomposition, supporting the interpretation that the dominant retained hydrogen

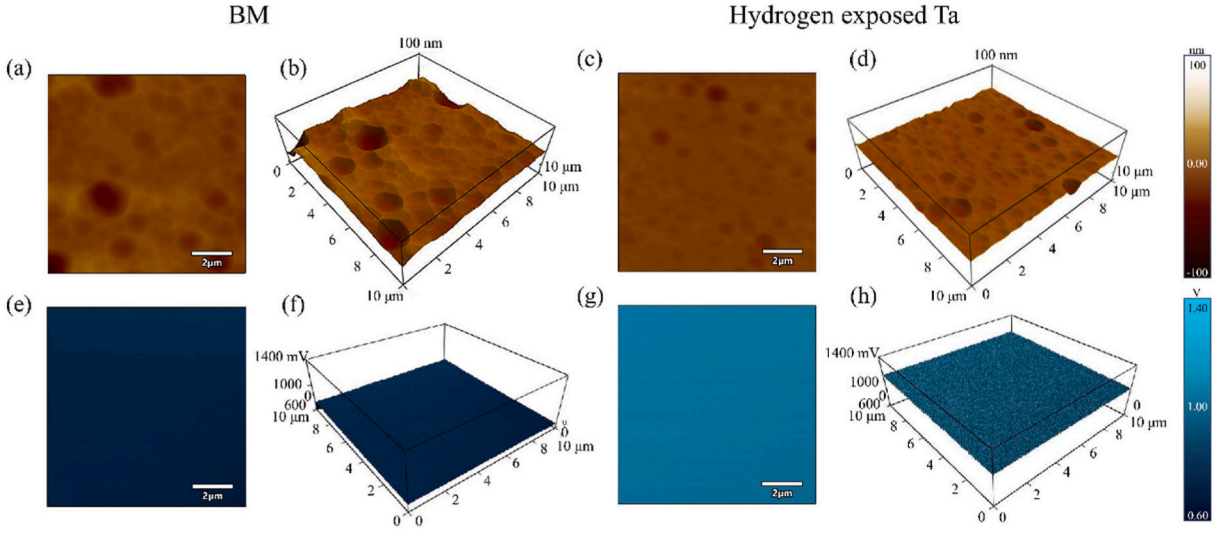

Fig. 8. 2D and 3D AFM topography of Ta surfaces: (a, b) BM and (c, d) Ta exposed to hydrogen at 600 °C; corresponding V_{CPD} maps of the same regions are shown in (e–h).

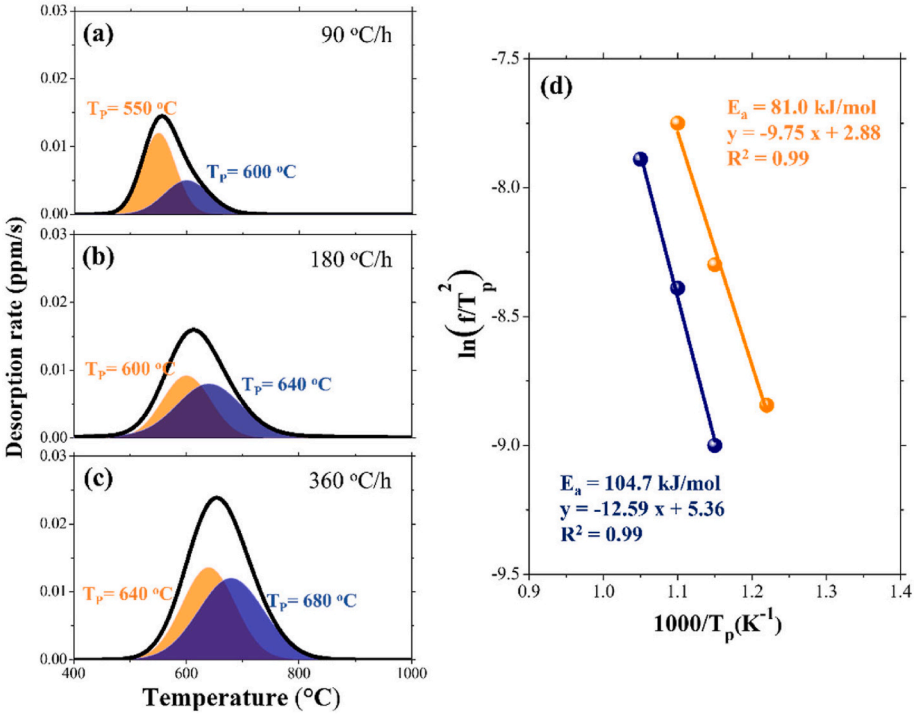

Fig. 9. TDS results of Ta exposed to hydrogen at 600 °C. Hydrogen desorption rate curves measured at heating rates of (a) 90, (b) 180, and (c) 360 °C h^{-1}, and (d) the corresponding Kissinger plots used to extract the apparent E_a of the hydrogen trapping states.

population is associated with reversible lattice and defect-related states rather than bulk hydride decomposition [39]. These results therefore suggest that hydrogen introduced during elevated-temperature exposure is retained in Ta primarily as dissolved lattice hydrogen together with hydrogen trapped at microstructural defects. Because these trapping states are relatively weak compared with hydride binding, hydrogen can be released readily as the temperature increases [65]. Despite this, the hydrogen content and surface hardness reached their maximum values at 600 °C (Fig. 4). This observation suggests that the increase in hydrogen ingress associated with the progressive destabilization of the surface oxide layer outweighed thermally activated hydrogen diffusion and desorption up to 600 °C, resulting in the highest retained hydrogen concentration and corresponding surface hardening at this temperature [69–71].

3.4. Tensile behavior

Based on the TDS and hardness results, the 600 °C condition, which exhibited the highest retained hydrogen content and surface hardness, was selected for tensile and DIC analyses. Although these tensile results alone do not establish the full temperature dependence of ductility, the comparison with the BM provides a representative assessment of the mechanical response associated with the most pronounced hydrogen uptake and hardening observed in this study. Fig. 10a compares the engineering stress–strain curves of the BM and the specimen exposed to hydrogen at 600 °C. Tensile tests were repeated three times to confirm reproducibility, and the corresponding mechanical properties are summarized in Table 1. The BM exhibits a typical ductile response characterized by a long uniform plastic deformation region followed by stable necking before fracture. In contrast, the hydrogen-exposed specimen shows a pronounced reduction in total elongation, indicating a clear loss

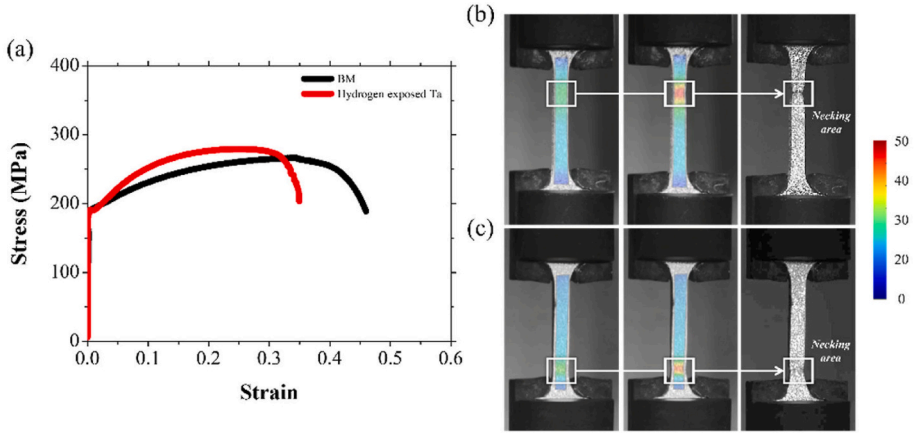

Fig. 10. Engineering stress–strain curves and DIC analysis of BM and hydrogen-exposed Ta specimens. (a) Engineering stress–strain curves of the BM and hydrogen-exposed Ta specimen at 600 °C. DIC strain distribution and fracture images of (b) the BM specimen and (c) the hydrogen-exposed Ta specimen at 600 °C. The color legend indicates the maximum strain, and the white rectangles highlight the strain evolution in the necking regions.

Table 1
Tensile test results of BM and Hydrogen exposed Ta.

	BM	Hydrogen exposed Ta
Yield Strength (MPa)	189.12 ± 3.54	191.24 ± 2.41
Ultimate Tensile Strength (MPa)	267.41 ± 5.43	279.13 ± 3.62
Elongation (%)	44.9 ± 6.54	34.6 ± 2.13
Strain energy (MJ/m^3)	111.3 ± 3.78	89.0 ± 7.21

of macroscopic ductility after elevated-temperature hydrogen exposure. The ultimate tensile strength increases only slightly from 267.41 ± 5.43 MPa for the BM to 279.13 ± 3.62 MPa after hydrogen exposure, whereas the strain energy decreases from 113.3 ± 3.78 to 89.0 ± 7.21 MJ m^{-3}. The modest change in strength accompanied by the pronounced reduction in elongation indicates that hydrogen exposure primarily degrades ductility rather than substantially strengthening the material. Assuming a uniform depth of detectable hydrogen-induced hardening of 90 μm from all four lateral surfaces of the 4 × 2 mm gauge cross-section, the hardened region occupies approximately 13.1% of the total cross-sectional area. Despite this limited area fraction, damage initiated in the near-surface region can generate local stress and strain concentrations and redistribute the load to the remaining ligament, thereby promoting strain localization and premature fracture. This provides a possible explanation for the observed macroscopic ductility loss without requiring uniform embrittlement throughout the specimen thickness.

DIC analysis further reveals clear differences in local deformation behavior. In the BM, the strain maps in Fig. 10b show a relatively broad and symmetric strain distribution across the gauge section, followed by the gradual development of a single necking region. In contrast, the hydrogen-exposed specimen exhibits more abrupt strain localization within a narrower region shortly before fracture, as shown in Fig. 10c. The localization occurs at a lower global strain, and the deformation becomes more strongly confined than in the BM. This behavior is consistent with the presence of dissolved hydrogen and hydrogen trapped at microstructural defects. These hydrogen states facilitate local stress concentration, destabilize plastic flow, and promote earlier strain localization and premature fracture [72,73]. As a result, the hydrogen-exposed specimen exhibits reduced ductility and lower strain energy, both of which are characteristic features of hydrogen-assisted embrittlement.

3.5. Fracture analysis

The fracture morphologies of the BM and the specimen exposed to hydrogen at 600 °C after tensile testing are shown in Figs. 11 and 12. The BM exhibits numerous dimples in the central region (Fig. 11a), indicative of a tensile-dominated fracture region formed via microvoid coalescence. These dimples result from the nucleation, growth, and coalescence of microvoids and are a classical feature of ductile fracture [74,75]. Toward the specimen edges (Fig. 11b), well-developed shear lips with a striated morphology are observed, reflecting shear-dominated plastic deformation that is typically present at the periphery of ductile tensile fractures. The coexistence of dimpled central regions and shear lips indicates that the BM undergoes a conventional ductile tensile fracture mechanism [76,77]. In contrast, the hydrogen-exposed specimen exhibits a markedly different fracture morphology. The central region (Fig. 12a) is dominated by quasi-cleavage facets, indicative of brittle-like tensile fracture behavior, with a significant reduction in both the number and size of dimples compared with the BM. At the specimen edges (Fig. 12b), quasi-cleavage features remain dominant rather than well-developed shear lips, indicating that shear-dominated plastic deformation is strongly suppressed. These facets interrupt the dimpled regions and reflect a reduced capacity for uniform plastic deformation during fracture [78,79]. This behavior is consistent with the DIC results, which showed enhanced strain localization and suppressed necking in the hydrogen-exposed specimen. The observed transition underscores the role of hydrogen in reducing ductility and promoting brittle fracture behavior in pure Ta [80]. Although hydrogen-induced hardening is concentrated near the surface, the hydrogen-affected surface layer and the less-affected core deform together during tensile loading, and differences in their resistance to plastic deformation may promote nonuniform strain partitioning [81,82]. This mechanical interaction may generate local stress and strain concentrations and promote crack growth into the specimen interior,

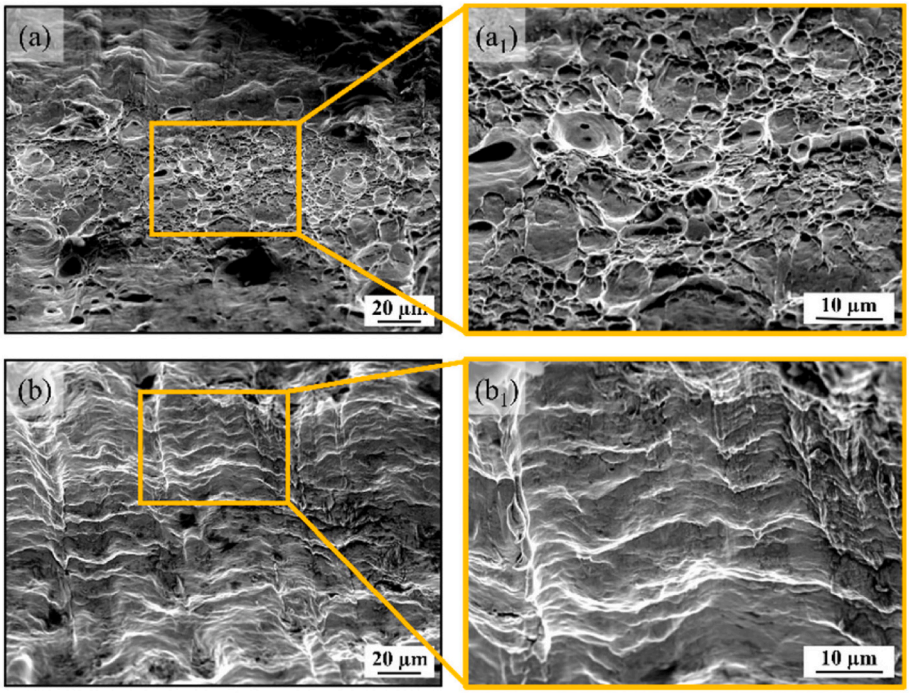

Fig. 11. Fracture surface analysis of the BM specimen after tensile testing. (a, b) Overall fracture morphologies, and (a_1, b_1) higher-magnification images of the regions marked by yellow boxes.

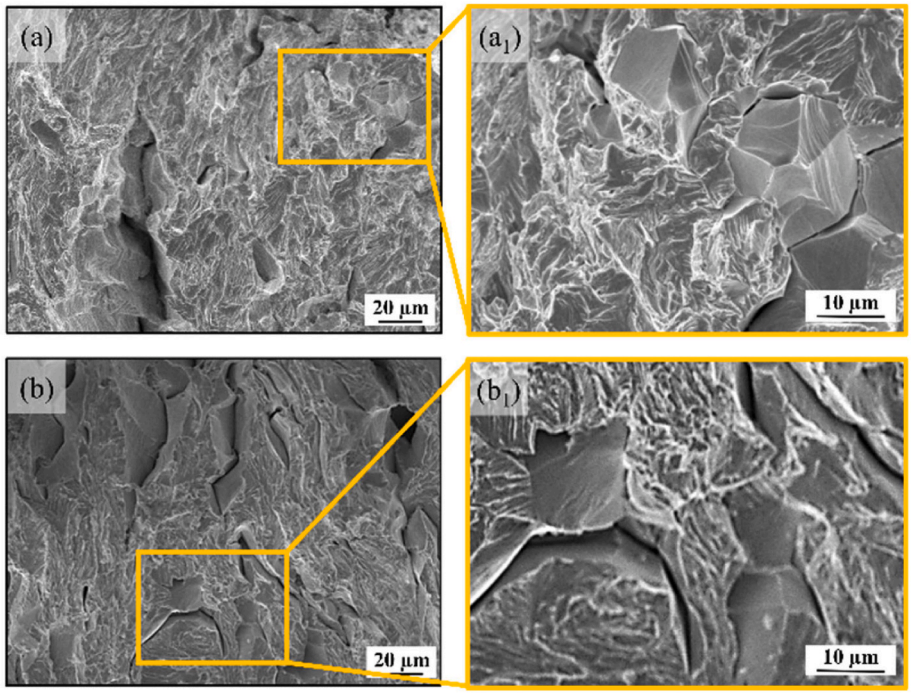

Fig. 12. Fracture surface analysis of the hydrogen-exposed specimen after tensile testing. (a, b) Overall fracture morphologies, and (a_1, b_1) higher-magnification images of the regions marked by yellow boxes.

thereby contributing to premature failure before the core fully develops its plastic deformation capacity.

4. Conclusions

This study investigates the effect of hydrogen exposure at elevated temperatures on the mechanical behavior and microstructural state of pure Ta. Specimens are exposed to hydrogen at 10 torr over a temperature range of 400–1000 °C, and the resulting changes in hardness, hydrogen content, lattice structure, microstructure, and tensile properties are systematically examined.

The hydrogen content measured by TDS exhibits a clear temperature dependence, reaching a maximum at 600 °C. The initial increase in hydrogen uptake between 400 and 600 °C may partly reflect enhanced hydrogen ingress associated with temperature-dependent changes in the native Ta_2O_5 barrier layer. At temperatures above 600 °C, the hydrogen content decreases due to reduced hydrogen trapping capacity resulting from thermally activated recovery, together with decreased equilibrium solubility and enhanced hydrogen diffusion. Correspondingly, the Vickers hardness shows a similar trend, increasing up to 600 °C and decreasing at higher temperatures.

XRD analysis shows a shift of diffraction peaks toward lower angles, indicating lattice expansion associated with interstitial hydrogen. SKPM measurements further reveal a reduction in surface work function after hydrogen exposure, providing evidence of electronic band structure modification due to interstitial hydrogen incorporation. EBSD observations show that the overall grain structure remains essentially unchanged after hydrogen exposure. TDS peak analysis at 600 °C suggests at least two retained-hydrogen states with different apparent thermal stabilities, consistent with hydrogen in dissolved and defect-associated states. These results support the interpretation that the retained hydrogen is predominantly present as interstitial and defect-associated hydrogen, although a possible contribution from nanoscale hydrides cannot be completely excluded.

Tensile testing demonstrates that hydrogen exposure at 600 °C results in a significant reduction in ductility and strain energy, with only a modest increase in strength. DIC analysis reveals earlier and more intense strain localization in the hydrogen-exposed specimen. Fractographic observations show a transition from predominantly dimpled ductile fracture in the BM to quasi-cleavage-dominated fracture after hydrogen exposure.

The maximum retained hydrogen content and surface hardness at 600 °C are observed under the present pressure, exposure duration, and cooling conditions. Higher hydrogen partial pressures are expected to increase the equilibrium concentration of dissolved hydrogen where Sieverts' law applies, but the resulting hydrogen retention and mechanical response also depend on hydrogen transport, trapping, and release. Accordingly, the magnitude and temperature dependence of hydrogen retention, as well as the relative contributions of different embrittlement mechanisms, may change at higher pressures. The present study provides a controlled experimental basis for understanding hydrogen-induced degradation following elevated-temperature exposure, while quantitative extrapolation to industrial hydrogen atmospheres requires pressure-dependent evaluation.

Data availability

The raw/processed data required to reproduce these findings cannot be shared at this time as the data also forms part of an ongoing study.

Declaration of competing interest

The authors declare that they have no known competing financial interests or personal relationships that could have appeared to influence the work reported in this paper.

Acknowledgment

This work was supported by Institute for Information & Communications Technology Promotion (IITP) grant funded by the Korea government (MSIP) (No.RS-2023-00222609). This research was supported by Nano·Material Technology Development Program through the National Research Foundation of Korea (NRF) funded by MSIT (RS-2025-02218040). This research was also supported by the ANCHOR

program through the Daejeon ANCHOR Center, funded by the Ministry of Education(MOE) and the Daejeon Metropolitan City, Republic of Korea (2026-ANCHOR-06-002). Hyojoo Lee was supported by the Korea Institute of Energy Technology Evaluation and Planning(KETEP) and the Ministry of Climate, Energy & Environment(MCEE) of the Republic of Korea (No. RS-2024- 00394769). Sangyeob Lee was supported by the National Research Foundation of Korea (NRF) grant funded by the Ministry of Science and ICT, Korea (RS-2025-23323229). Jungho Shin was supported by the Korea Planning & Evaluation Institute of Industrial Technology (KEIT) and the Ministry of Trade, Industry & Energy (MOTIE) of the Republic of Korea (RS-2024-00432864).

References

[1] Kumar S, Singh A, Jain U, Dey GK. Development of tantalum–zirconium alloy for hydrogen purification. Fusion Eng Des 2016;109–111:1487–90. https://doi.org/10.1016/j.fusengdes.2015.11.047.
[2] Gramberg U, Renner M, Diekmann H. Tantalum as a material of construction for the chemical processing industry – a critical survey. Mater Corros 1995;46:689–700. https://doi.org/10.1002/maco.19950461206.
[3] Agrawal M, Singh R, Ranitović M, Kamberovic Z, Ekberg C, Singh KK. Global market trends of tantalum and recycling methods from waste tantalum capacitors: a review. Sustain Mater Technol 2021;29:e00323. https://doi.org/10.1016/j.susmat.2021.e00323.
[4] Baton J, Geslin W, Moussa C. Influence of pre-recovery on the recrystallization of pure tantalum. J Mater Sci 2021;56:15354–78. https://doi.org/10.1007/s10853-021-06218-0.
[5] Wei X, Xia LG, Liu ZH, Zhang LR, Li QH. A review of tantalum resources and its production. Trans Nonferrous Met Soc China 2023;33:3132–56. https://doi.org/10.1016/S1003-6326(23)66323-X.
[6] Hydrogen Damage and Embrittlement. Failure analysis and prevention. ASM International; 2002. p. 809–22. https://doi.org/10.31399/asm.hb.v11.a0003552.
[7] Ensinger W, Flege S, Baba K. Platinum implantation into tantalum for protection against hydrogen embrittlement during corrosion. Nucl Instrum Methods Phys Res B 2012;272:441–5. https://doi.org/10.1016/j.nimb.2011.01.119.
[8] Mattox DM. Surface preparation for film and coating deposition processes. Handbook of Deposition Technologies for Films and Coatings 2010:93–134. https://doi.org/10.1016/B978-0-8155-2031-3.00003-X.
[9] Birnbaum HK, Sofronis P. Hydrogen-enhanced localized plasticity—a mechanism for hydrogen-related fracture. Mater Sci Eng A 1994;176:191–202. https://doi.org/10.1016/0921-5093(94)90975-X.
[10] Lynch S. Hydrogen embrittlement phenomena and mechanisms. Corros Rev 2012;30:105–23. https://doi.org/10.1515/corrrev-2012-0502.
[11] Chandler WT, Walter RJ. Hydrogen effects in refractory metals. Refractory metal alloys metallurgy and technology. 1968. p. 197–249. https://doi.org/10.1007/978-1-4684-9120-3_6.
[12] Hossick-Schott J, Reiterer M, Heffelfinger J, Hintz M, Ringle M, Levina I, Gaffney K. Latent cracking of tantalum–titanium welds due to hydrogen embrittlement. JOM 2013;65:625–9. https://doi.org/10.1007/s11837-013-0582-7.
[13] Yang B, Qin G, Fu B, Li CA, Wang H. Advances in welding of tantalum alloy. J Mater Res Technol 2025;38:5052–81. https://doi.org/10.1016/j.jmrt.2025.08.277.
[14] Lusby WE. Titanium, zirconium and tantalum for control of corrosion. Corrosion 1957;13:56–60. https://doi.org/10.5006/0010-9312-13.10.56.
[15] Taxak M, Krishnamurthy N. Effect of aluminum on hydrogen absorption kinetics of tantalum. J Alloys Compd 2015;623:121–6. https://doi.org/10.1016/j.jallcom.2014.10.064.
[16] Wriedt HA, Oriani RA. The effect of hydrogen on the Young's modulus of tantalum, niobium and vanadium. Scripta Metall 1974;8:203–8. https://doi.org/10.1016/0036-9748(74)90239-7.
[17] Wei Z, Huang L, Guan K, Zhong J. Failure of a tantalum lined tee induced by hydrogen embrittlement. Eng Fail Anal 2025;167:108969. https://doi.org/10.1016/j.engfailanal.2024.108969.
[18] Semboshi S, Masahashi N, Hanada S. Hydrogenation-induced fragmentation in Ta–Ni alloy. J Alloys Compd 2003;359:236–43. https://doi.org/10.1016/S0925-8388(03)00200-7.
[19] Spitzig WA, Owen CV, Scott TE. The effects of interstitials and hydrogen–interstitial interactions on low-temperature hardening and embrittlement in V, Nb, and Ta. Metall Mater Trans A 1986;17:1179–89. https://doi.org/10.1007/BF02665317.
[20] Owen CV, Scott TE. Relation between hydrogen embrittlement and the formation of hydride in the group V transition metals. Metall Mater Trans A 1972;3:1715–26. https://doi.org/10.1007/BF02642552.
[21] Walter RJ, Beetle GG, Chandler WT. Effect of water vapor/hydrogen environments on niobium, B-66 niobium alloy, tantalum, and Ta–10W alloy. Corrosion 1991;47:272–80. https://doi.org/10.5006/1.3585255.
[22] Ensinger W. Ion-beam sputter coating of tantalum tube inner walls for protection against hydrogen embrittlement. Surf Coat Technol 1996;84:434–8. https://doi.org/10.1016/S0257-8972(95)02763-7.
[23] ASTM E8/E8M. Standard test methods for tension testing of metallic materials. Annu Book ASTM (Am Soc Test Mater) Stand 2010;4:1–27. https://doi.org/10.1520/E0008.
[24] Nechaev YS, Denisov EA, Shurygina NA, Cheretaeva AO, Kostikova EK, Davydov SY, Öchsner A. Revealing hydrogen States in carbon structures by analyzing the thermal desorption spectra. C-Journal of Carbon Research 2022;8. https://doi.org/10.3390/c8010006.
[25] Hammer P, Peil OE, Azizpour A, Vandewalle L, Verbeken K, Depover T, Razumovskiy VI. The fingerprint method for analysis of thermal desorption spectra. npj Mater Degrad 2026;10. https://doi.org/10.1038/s41529-025-00718-z.
[26] Mathieu HJ, Datta M, Landolt D. Thickness of natural oxide films determined by AES and XPS with/without sputtering. J Vac Sci Technol A 1985;3:331–5. https://doi.org/10.1116/1.573260.
[27] Wolf MJ, Roitsch S, Mayer J, Nijmeijer A, Bouwmeester HJM. Fabrication of ultrathin films of Ta_2O_5 by a sol-gel method. Thin Solid Films 2013;527:354–7. https://doi.org/10.1016/j.tsf.2012.12.054.
[28] Stewart DA. Diffusion of oxygen in amorphous tantalum oxide. Phys Rev Mater 2019;3. https://doi.org/10.1103/PhysRevMaterials.3.055605.
[29] Lu CH, Wu CH. Low-temperature crystallization of tantalum pentoxide films under elevated pressure. J Eur Ceram Soc 2006;26:2753–9. https://doi.org/10.1016/j.jeurceramsoc.2005.07.054.
[30] Skaja KJ. Redox processes and ionic transport in resistive switching binary metal oxides. RWTH Aachen University; 2016. Ph.D. thesis.
[31] Mine Y, Tsumagari T, Horita Z. Hydrogen trapping on lattice defects produced by high-pressure torsion in Fe–0.01 mass% C alloy. Scr Mater 2010;63:552–5. https://doi.org/10.1016/j.scriptamat.2010.05.027.
[32] Turk A, Joshi GR, Gintalas M, Callisti M, Rivera-Díaz-del-Castillo PEJ, Galindo-Nava EI. Quantification of hydrogen trapping in multiphase steels: part I – point traps in martensite. Acta Mater 2020;194:118–33. https://doi.org/10.1016/j.actamat.2020.05.007.
[33] Caravella A, Hara S, Drioli E, Barbieri G. Sieverts law pressure exponent for hydrogen permeation through Pd-based membranes: coupled influence of non-ideal diffusion and multicomponent external mass transfer. Int J Hydrogen Energy 2013;38:16229–44. https://doi.org/10.1016/j.ijhydene.2013.09.102.
[34] Taxak M, Kumar S, Kalekar BB, Krishnamurthy N. Effect of nickel addition on the solubility of hydrogen in tantalum. Int J Hydrogen Energy 2013;38:7561–8. https://doi.org/10.1016/j.ijhydene.2013.03.155.
[35] Taxak M, Kumar S, Sheelvantra S, Krishnamurthy N. Effect of iron on the solubility of hydrogen in tantalum. J Mater Sci 2014;49:8471–7. https://doi.org/10.1007/s10853-014-8557-9.
[36] Taxak M, Kumar S, Krishnamurthy N, Suri A, Tiwari G. Change in lattice parameter of tantalum due to dissolved hydrogen. Process Appl Ceram 2012;6:73–6. https://doi.org/10.2298/PAC1202073T.
[37] Franzen HF, Khan AS, Peterson DT. The solubility of hydrogen in tantalum at high temperatures. J Less Common Met 1977;55:143–7. https://doi.org/10.1016/0022-5088(77)90273-9.
[38] Rokhmanenkov A, Yanilkin A. Simulation of hydrogen thermal desorption and stability of titanium hydrides TiHx. Int J Hydrogen Energy 2019;44:29132–9. https://doi.org/10.1016/j.ijhydene.2019.03.237.
[39] Chen YS, Huang C, Liu PY, Yen HW, Niu R, Burr P, Moore KL, Martínez-Pañeda E, Atrens A, Cairney JM. Hydrogen trapping and embrittlement in metals: a review. Int J Hydrogen Energy 2025;136:789–821. https://doi.org/10.1016/j.ijhydene.2024.04.076.
[40] Stüwe HP, Padilha AF, Siciliano Jr F. Competition between recovery and recrystallization. Mater Sci Eng A 2002;333:361–7. https://doi.org/10.1016/S0921-5093(01)01860-3.
[41] Liu X, Zhang P, Zhan M, Dang B, Yang K, Han P. Capture and diffusion of hydrogen in tantalum and copper with vacancy defects: a first-principles study. ACS Appl Mater Interfaces 2025;17:2376–88. https://doi.org/10.1021/acsami.4c13331.
[42] Yamanaka S, Fujita Y, Uno M, Katsura M. Influence of interstitial oxygen on hydrogen solubility in metals. J Alloys Compd 1999;293–295:42–51. https://doi.org/10.1016/S0925-8388(99)00398-9.
[43] Huang C, Cui C, Niu R, Lu F, Wu CY, Zhu X, Lu H, Zhang Y, Liu PY, Dong B, Sun YH, Wang H, Li W, Yen HW, Guo A, Cairney JM, Martínez-Pañeda E, Chen EYS. Strong hydrogen trapping by tangled dislocations in cold-drawn pearlitic steels. Acta Mater 2025;296:121231. https://doi.org/10.1016/j.actamat.2025.121231.
[44] Wada K, Yamabe J, Matsunaga H. Mechanism of hydrogen-induced hardening in pure nickel and in a copper–nickel alloy analyzed by micro vickers hardness testing. Mater Sci Eng A 2021;805:140580. https://doi.org/10.1016/j.msea.2020.140580.
[45] Murakami Y, Kanezaki T, Mine Y. Hydrogen effect against hydrogen embrittlement. Metall Mater Trans A 2010;41:2548–62. https://doi.org/10.1007/s11661-010-0275-6.
[46] Yamabe J, Wada K, Awane T, Matsunaga H. Hydrogen distribution of hydrogen-charged nickel analyzed via hardness test and secondary ion mass spectrometry. Int J Hydrogen Energy 2020;45:9188–99. https://doi.org/10.1016/j.ijhydene.2020.01.117.
[47] Mathaudhu SN, Hartwig KT. Grain refinement and recrystallization of heavily worked tantalum. Mater Sci Eng A 2006;426:128–42. https://doi.org/10.1016/j.msea.2006.03.089.
[48] Fan J, Zhu Y, Wang W, Chen K, Godfrey A, Yu T, Huang X. Recovery of dislocation cell structures in 316L stainless steel manufactured by selective laser melting. J Mater Res Technol 2024;30:9472–80. https://doi.org/10.1016/j.jmrt.2024.05.269.
[49] Pouraliakbar H, Jandaghi MR, Aval HJ, Shim SH, Moverare J, Na YS, Khalaj G, Fallah V. An EBSD study on microstructure and texture development in graphene-

reinforced i nanocomposites via FSP. J Mater Res Technol 2025;35:685–701. https://doi.org/10.1016/j.jmrt.2024.12.190.
[50] Kamaya M. Assessment of local deformation using EBSD: quantification of accuracy of measurement and definition of local gradient. Ultramicroscopy 2011;111:1189–99. https://doi.org/10.1016/j.ultramic.2011.02.004.
[51] Rui SS, Han QN, Wang X, Li S, Ma X, Su Y, Cai Z, Du D, Shi HJ. Correlations between two EBSD-Based metrics Kernel Average misorientation and image quality on indicating dislocations of near-failure low alloy steels induced by tensile and cyclic deformations. Mater Today Commun 2021;27:102445. https://doi.org/10.1016/j.mtcomm.2021.102445.
[52] Pfeiffer H, Peisl H. Lattice expansion of niobium and tantalum due to dissolved hydrogen and deuterium. Phys Lett A 1977;60:363–4. https://doi.org/10.1016/0375-9601(77)90129-3.
[53] Grena R, Celino M, Tarquini P. DFT study of interstitial hydrogen in tantalum lattice. Int J Hydrogen Energy 2011;36:13858–65. https://doi.org/10.1016/j.ijhydene.2011.07.130.
[54] Oates WA, Flanagan TB. The terminal solubility of hydrogen in niobium–tantalum alloys. Acta Metall 1985;33:693–7. https://doi.org/10.1016/0001-6160(85)90033-1.
[55] Kuzovnikov MA, Antonov VE, Ivanov AS, Hansen T, Savvin S, Kulakov VI, Tkacz M, Kolesnikov AI. Neutron scattering study of tantalum monohydride and monodeuteride. Int J Hydrogen Energy 2021;46:20630–9. https://doi.org/10.1016/j.ijhydene.2021.03.149.
[56] Glatzel T, Gysin U, Meyer E. Kelvin probe force microscopy for material characterization. Microscopy 2022;71:I165–73. https://doi.org/10.1093/jmicro/dfab040.
[57] Melitz W, Shen J, Kummel AC, Lee S. Kelvin probe force microscopy and its application. Surf Sci Rep 2011;66:1–27. https://doi.org/10.1016/j.surfrep.2010.10.001.
[58] Juan A, Moro L, Brizuela G, Pronsato E. The electronic structure and bonding of a hydrogen pair near an FCC Fe stacking fault. Int J Hydrogen Energy 2002;27:333–8. https://doi.org/10.1016/S0360-3199(01)00113-6.
[59] Gonzalez EA, Jasen PV, Castellani NJ, Juan A. The effect of interstitial hydrogen on the electronic structure of Fe–Pd alloys. J Phys Chem Solid 2004;65:1799–807. https://doi.org/10.1016/j.jpcs.2004.05.008.
[60] Switendick AC. Metal hydrides—Structure and band structure. Int J Quant Chem 1971;5:459–70. https://doi.org/10.1002/qua.560050854.
[61] Peterman DJ, Misemer DK, Weaver JH, Peterson DT. Electronic structure of metal hydrides. VI. Photoemission studies and band theory of VH, NbH, and TaH. Phys Rev B 1983;27:799–807. https://doi.org/10.1103/PhysRevB.27.799.
[62] Ryu JH, Chun YS, Lee CS, Bhadeshia HKDH, Suh DW. Effect of deformation on hydrogen trapping and effusion in TRIP-assisted steel. Acta Mater 2012;60:4085–92. https://doi.org/10.1016/j.actamat.2012.04.010.
[63] Yan F, Mouton I, Stephenson LT, Breen AJ, Chang Y, Ponge D, Raabe D, Gault B. Atomic-scale investigation of hydrogen distribution in a Ti–Mo alloy. Scr Mater 2019;162:321–5. https://doi.org/10.1016/j.scriptamat.2018.11.040.
[64] Chen L, Xiong X, Tao X, Su Y, Qiao L. Effect of dislocation cell walls on hydrogen adsorption, hydrogen trapping and hydrogen embrittlement resistance. Corros Sci 2020;166:108428. https://doi.org/10.1016/j.corsci.2020.108428.
[65] Xu Z, Zhu Y, Liu S, Li W, Chen J, Gao K, Shi R, Pang X. Effect of Laves-decorated dendrite structure on hydrogen embrittlement in selective laser-melted nickel-based alloy. J Mater Sci Technol 2025;239:1–15. https://doi.org/10.1016/j.jmst.2025.03.051.
[66] Schmid K, Rieger V, Manhard A. Comparison of hydrogen retention in W and W/Ta alloys. J Nucl Mater 2012;426:247–53. https://doi.org/10.1016/j.jnucmat.2012.04.003.
[67] Azarenkov MO, Bobkov VV, Tishchenko LP, Kovtunenko YI, Skrypnyk AO, Shevchenko DI, Gamayunova LO. Investigation of the processes of retention and release of implanted deuterium and helium ions for tungsten and tantalum coatings. East Eur J Phys 2024;2024:10–30. https://doi.org/10.26565/2312-4334-2024-1-01.
[68] International Atomic Energy Agency. Atomic and plasma–material interaction data for fusion, vol. 16. Vienna: IAEA; 2014.
[69] Drexler A, Helic B, Silvayeh Z, Mraczek K, Sommitsch C, Domitner J. The role of hydrogen diffusion, trapping and desorption in dual phase steels. J Mater Sci 2022;57:4789–805. https://doi.org/10.1007/s10853-021-06830-0.
[70] Gao Z, Lee DH, Zhao Y, Wang P, Murakami K, Komazaki SI, Suh JY, Kim HS, Ramamurty U, Jang JI. Hydrogen trapping and micromechanical behavior in additively manufactured CoCrFeNi high-entropy alloy in as-built and pre-strained conditions. Acta Mater 2024;271:119886. https://doi.org/10.1016/j.actamat.2024.119886.
[71] Wright DA. Absorption of gases by tantalum. Nature 1938;142:794. https://doi.org/10.1038/142794a0.
[72] Song J, Curtin WA. A nanoscale mechanism of hydrogen embrittlement in metals. Acta Mater 2011;59:1557–69. https://doi.org/10.1016/j.actamat.2010.11.019.
[73] Martin ML, Dadfarnia M, Nagao A, Wang S, Sofronis P. Enumeration of the hydrogen-enhanced localized plasticity mechanism for hydrogen embrittlement in structural materials. Acta Mater 2019;165:734–50. https://doi.org/10.1016/j.actamat.2018.12.014.
[74] Das A. Effect of phase interfaces to dimple pattern. Mater Lett 2023;337:133954. https://doi.org/10.1016/j.matlet.2023.133954.
[75] Noell PJ, Carroll JD, Boyce BL. The mechanisms of ductile rupture. Acta Mater 2018;161:83–98. https://doi.org/10.1016/j.actamat.2018.09.006.
[76] Boyce BL, Clark BG, Lu P, Carroll JD, Weinberger CR. The morphology of tensile failure in tantalum. Metall Mater Trans A 2013;44:4567–80. https://doi.org/10.1007/s11661-013-1814-8.
[77] Xue L, Wierzbicki T. Ductile fracture initiation and propagation modeling using damage plasticity theory. Eng Fract Mech 2008;75:3276–93. https://doi.org/10.1016/j.engfracmech.2007.08.012.
[78] Merson ED, Myagkikh PN, Poluyanov VA, Merson DL, Vinogradov A. Quasi-cleavage hydrogen-assisted cracking path investigation by fractographic and side surface observations. Eng Fract Mech 2019;214:177–93. https://doi.org/10.1016/j.engfracmech.2019.04.042.
[79] Cho L, Bradley PE, Lauria DS, Martin ML, Connolly MJ, Benzing JT, Seo EJ, Findley KO, Speer JG, Slifka AJ. Characteristics and mechanisms of hydrogen-induced quasi-cleavage fracture of lath martensitic steel. Acta Mater 2021;206:116635. https://doi.org/10.1016/j.actamat.2021.116635.
[80] Martin ML, Fenske JA, Liu GS, Sofronis P, Robertson IM. On the formation and nature of quasi-cleavage fracture surfaces in hydrogen-embrittled steels. Acta Mater 2011;59:1601–6. https://doi.org/10.1016/j.actamat.2010.11.024.
[81] Örnek C, Larsson A, Harlow GS, Zhang F, Kroll R, Carlà F, Hussain H, Kivisäkk U, Engelberg DL, Lundgren E, Pan J. Time-resolved grazing-incidence X-ray diffraction measurement to understand the effect of hydrogen on surface strain development in super duplex stainless steel. Scr Mater 2020;187:63–7. https://doi.org/10.1016/j.scriptamat.2020.05.061.
[82] Pogrielz T, Eichinger M, Weiser A, Todt J, Hohenwarter A, Ascii A, Sarac B, Brandl D, Ressel G, Jary M, Dlouhy A, Mori G, Keckes J. Peculiarity of hydrogen absorption in duplex steels: Phase-selective lattice swelling and stress evolution. Scr Mater 2024;248:116142. https://doi.org/10.1016/j.scriptamat.2024.116142.